ELSEVIER

#### Contents lists available at ScienceDirect

# Acta Materialia

journal homepage: www.elsevier.com/locate/actamat



# Full length article

# Predicting the early-stage creep dynamics of gels from their static structure by machine learning



Han Liu<sup>a</sup>, Siqi Xiao<sup>a,b</sup>, Longwen Tang<sup>a</sup>, Enigma Bao<sup>a,c</sup>, Emily Li<sup>a,c</sup>, Caroline Yang<sup>a,c</sup>, Zhangji Zhao<sup>a</sup>, Gaurav Sant<sup>d,e</sup>, Morten M. Smedskjaer<sup>f</sup>, Lijie Guo<sup>g</sup>, Mathieu Bauchy<sup>a,\*</sup>

- <sup>a</sup> Physics of AmoRphous and Inorganic Solids Laboratory (PARISlab), Department of Civil and Environmental Engineering, University of California, Los Angeles, CA 90095, United States
- <sup>b</sup> College of Civil Engineering, Tongji University, Shanghai 200092, China
- <sup>c</sup> Department of Statistics, University of California, Los Angeles, CA, 90095, United States
- d Laboratory for the Chemistry of Construction Materials (LC<sup>2</sup>), Department of Civil and Environmental Engineering, University of California, Los Angeles, CA 90095, United States
- e California Nanosystems Institute (CNSI), University of California, Los Angeles, CA 90095, United States
- f Department of Chemistry and Bioscience, Aalborg University, Aalborg 9220, Denmark
- g National Centre for International Research on Green Metal Mining, BGRIMM Technology Group, Beijing 100160, China

#### ARTICLE INFO

# Article history: Received 5 September 2020 Revised 15 March 2021 Accepted 15 March 2021 Available online 22 March 2021

Keywords:
Colloidal gels
Viscoplastic deformations
Accelerated molecular dynamics
Machine learning

#### ABSTRACT

Upon sustained loading, colloidal gels tend to feature delayed viscoplastic creep deformations. However, the relationship, if any, between the structure and creep dynamics of gels remains elusive. Here, based on accelerated molecular dynamics simulations and the recently developed softness approach (i.e., classification-based machine learning), we reveal that the propensity of a gel to exhibit long-time creep is encoded in its static, unloaded structure. By taking the example of a calcium-silicate-hydrate gel (the binding phase of concrete), we extract a local, non-intuitive structural descriptor (a revised version of the "softness" metric proposed by the pioneering work from Cubuk *et al.*) that is strongly correlated with the dynamics of the particles. Notably, the macroscopic creep rate exhibits an exponential dependence on the average softness. We find that creep results in a decrease in softness in the gel structure, which, in turn, explains the gradual decay of the creep rate over time. Finally, we demonstrate that the softness metric is strongly correlated with the average energy barrier that is accessible to the particles.

© 2021 Acta Materialia Inc. Published by Elsevier Ltd. All rights reserved.

# 1. Introduction

When subjected to a sustained load, disordered solids (e.g., glasses, granular materials, or gels) tend to exhibit delayed, time-dependent creep deformations [1–3]. Although creep can occur in many types of materials (e.g., metals or ceramics, primarily at high temperature [4,5]), it is especially pronounced in soft matter, e.g., colloidal gels [3,6,7]. In that regard, the viscoplastic deformation of calcium–silicate–hydrate gels (C–S–H, the binding phase of concrete) under constant load plays a key role in the built environment since it is responsible for concrete's creep [7–10].

Despite the important, often detrimental role of creep in colloidal gels, its nanoscale origin, driving force, and mechanism remain debated [3,6,8]. In particular, it remains unclear whether the propensity of a disordered solid to creep could in some way be encoded in its static, unloaded structure [11]. This question is a mani-

\* Corresponding author.

E-mail address: bauchy@ucla.edu (M. Bauchy).

festation of a more general gap in our understanding of how structure controls dynamics in disordered phases [6,11,12]. Indeed, due to the complex, disordered structure of glasses or gels [13,14], pinpointing which structural features govern dynamics is essentially a "needle-in-a-haystack" problem [15–17], since intuitive structural metrics (e.g., local packing or coordination number) are often only weakly correlated with dynamics [18,19].

Owing to its ability to discover relevant patterns in complex, multidimensional data, machine learning (ML) offers a new opportunity to revisit the nature of the linkages between structure and dynamics in disordered phases—without the need for any prerequisite intuition regarding which structural feature(s) could be influential [20,21]. In particular, Cubuk *et al.* recently extracted by ML a non-intuitive structural fingerprint (named "softness"), which is strongly correlated with the probability of a particle to exhibit some rearrangement upon loading or spontaneous relaxation [12,15,22–26]. However, although softness has been shown to be correlated with near-future particle rearrangements, it has thus far been unable to offer insights into the long-time dynamics of

disordered phases [11]. This has prevented the use of this approach to study creep, which can extend over several years [9].

Here, inspired by this softness approach, we introduce a slightly revised definition for softness (relying on a linear logistic regression model and radial features) and use this machine-learned structural fingerprint to interrogate the existence of a causal link between structure and long-time creep. This approach reveals that the propensity of a colloidal gel to creep is encoded in its instantaneous, static structure. Importantly, we find that the softness metric captures the effective average energy barrier that the particles need to overcome to rearrange during creep—which suggests that the softness metric offers a structural fingerprint of the topography of the energy landscape. Finally, the use of linear logistic regression allows us to offer a structural interpretation of this machine-learned predictor.

#### 2. Methods

#### 2.1. Archetypical gel model

To establish our conclusions, we simulate an archetypical mesoscale model of a colloidal C–S–H gel [10,27,28]. The model gel is comprised of an ensemble of monodisperse spherical particles of 5 nm. The interaction between particles is described by a generalized Lennard-Jones potential with a minimum at distance  $\sigma = \sqrt[14]{2} \times 5$  nm, which corresponds to the effective particle diameter. In detail, the potential is descried as [27]:

$$U_{ij}(r_{ij}) = 4\varepsilon \left[ \left( \frac{\sigma_0}{r_{ij}} \right)^{2\alpha} - \left( \frac{\sigma_0}{r_{ij}} \right)^{\alpha} \right]$$
 (1)

where  $\sigma_0$  is the particle diameter (5 nm here),  $\alpha$  a parameter that controls the narrowness of the potential well (here,  $\alpha=14$ ),  $r_{ij}$  the distance between the centers of a pair of particles i and j, and  $\varepsilon$  the depth of the potential energy well and  $\varepsilon=A_0\sigma_0^3$ , where  $A_0=kE$  is a prefactor that is proportional to the Young's modulus E of a bulk C–S–H grain (here, E=63.6 GPa and k=0.002324). The potential defined in Eq. (1) exhibits a minimum at  $r_m=\sqrt[\alpha]{2}\sigma_0$  so that the effective diameter of a particle i is here defined as  $\sigma=\sqrt[\alpha]{2}\sigma_0$ . This model has been extensively studied and has been shown to offer a realistic description of the structure and mechanical properties of C–S–H gels [8,10,27–31].

# 2.2. Preparation of the gel configurations

The gel configurations are generated by grand canonical Monte Carlo (GCMC) simulations, wherein particles are iteratively inserted until saturation into an initially empty cubic box of 600 Å length with periodic boundary. Each GCMC step comprises of 5 attempts of particle insertions or deletions, followed by 500 attempts of random displacement of an existing particle. The temperature is fixed at T = 300 K and the excess chemical potential, controlling the probability of acceptance of the insertion attempts, is set to  $-2k_BT$ . In detail, the probability of acceptance of the attempt is given by min{1,  $\exp[-(\Delta U - \mu \delta)/k_B T]$ }, where  $k_B$  is the Boltzmann constant, T the temperature,  $\Delta U$  the variation in potential energy caused by the trial move,  $\mu$  the chemical potential (fixed at  $-2k_BT$  based on Refs. [8,10,27–31], which ensures the formation of a realistic packed final structure within a reasonable simulation time), and  $\delta$  the variation in the number of C-S-H grains [8,28,29]. The saturated configurations are then relaxed by molecular dynamics (MD) simulations with a timestep of 50 fs in the isothermal-isobaric (NPT) ensemble at 300 K and zero stress for 50 ns to release the macroscopic tensile pressure formed during the GCMC simulation. Finally, the configurations are subjected to an energy minimization to reach their inherent structure. Note that the GCMC ensemble adopted herein aims to mimic the precipitation process of colloidal C–S–H gels and has been shown to offer a realistic description of the structure and packing density of disordered C–S–H gels [8,10,27–31]. Based on the system size considered herein, we typically get a number of particles  $n_p \approx 1700$  at saturation, which corresponds to a packing density  $\varphi \approx 0.63$ . Using this methodology, we simulate 10 independent configurations for statistical averaging. All simulations are performed by using the Large-scale Atomic/Molecular Massively Parallel Simulator (LAMMPS) code [32].

#### 2.3. Accelerated creep simulations

Since a direct MD simulation of the creep of colloidal gels is out of reach considering its extended timescale, we adopt herein a recently introduced accelerated simulation technique [33,34], which has been shown to successfully model the creep of disordered phases [2.8]. This accelerated method relies on the application of small stress perturbations to accelerate relaxation [2,33,34]. In detail, we first apply a constant, sustained shear stress  $\tau_0$  (here  $\tau_0 = 100$  MPa) to induce a creep response within the gel. The creep response of the gel is simply a linear function of  $\tau_0$ , as long as  $\tau_0$  remains lower than the yield stress of the gel [8]. Small, cyclic shear stress perturbations  $\pm \Delta \tau$  (here  $\Delta \tau = 30$  MPa) are then applied to accelerate the creep dynamics [8]. At each stress cycle, a constant-stress minimization of the energy is performed, wherein the system can adjust its shape and volume in order to reach the target stress. Effectively, this method mimics the accelerated relaxation exhibited by granular materials when subjected to vibrations [35]. The resulting acceleration of the dynamics arises from the fact that each stress perturbation slightly deforms the local energy landscape, which, in turn, can reduce the height of some energy barriers that are locally accessible to the particles. This allows the system to jump over these barriers, thereby reaching a new energy basin within the landscape in an accelerated fashion [2,33,36]. Such particle reorganizations make it possible for the gel to exhibit some macroscopic viscoplastic deformation (i.e., creep) in order to accommodate the external sustained shear stress. Note that the average stress  $\tau_0$  of 100 MPa used herein is notably lower than the yield stress of the system (~600 MPa), so that no macroscopic flow of particles is observed. In addition, the stress perturbation amplitude  $\Delta \tau$  ( $\pm$  30 MPa) is chosen to be large enough to accelerate the creep simulation, but low enough to avoid any rejuvenation [8]. The resulting creep modulus was shown to be independent of the specific value of this stress perturbation amplitude  $\Delta \tau$  [8]. It is worth pointing out that, in practice, our accelerated simulation technique mimics a dynamical fatigue test-wherein a series of oscillatory stresses are repeatedly applied to the simulated sample. Nevertheless, when the applied stress is low as compared to the yield stress, the resulting logarithmic strain deformation of the simulated sample is effectively equivalent to the one that is experimentally observed upon non-oscillatory static loading test (i.e., creep) [37,38]. Since the particle rearrangements induced by the stress perturbations are limited, the modeled gel remains in the primary creep stage (i.e., wherein the creep rate decays over time) without entering into the secondary steady-state stage (i.e., constant creep rate) or the final avalanche stage (i.e., acceleration of creep rate) [39,40]. It should also be noted that the monodisperse colloidal gel considered herein is out-of-equilibrium and tends to easily crystalize at finite temperature. Nevertheless, no crystallization is observed during the creep simulations. All simulations are performed by using the LAMMPS code [32].

# 2.4. Non-affine squared displacement of the particles

We calculate, for each particle i, the normalized non-affine squared displacement  $D^2_{min}/\sigma^2$  at the Nth stress perturbation

cycle (here,  $N=10^6$ ) with respect to the initial reference configuration (here,  $N_{\text{ref}}=1$ ) using Eq. (2) [22,41]:

$$D_{\min}^2/\sigma^2(i, N, N_{\text{ref}}) = \frac{\min_{\Lambda_i} \left\{ \frac{1}{n_i} \sum_{j} \left[ R_{ij}(N) - \Lambda_i R_{ij}(N_{\text{ref}}) \right]^2 \right\}}{\sigma^2}$$
(2)

where  $R_{ij}$  is the distance between particle i and j, particle j represents the neighbor of particle i within a cutoff distance  $R_c$  (here,  $R_c = 2\sigma$  [41]), and  $n_i$  is the total number of neighbor particles within the range of  $R_c$  for each particle i. The quantity is minimized over choices of the local strain tensor  $\Lambda_i$  of particle i. Note that the quantity  $\Lambda_i R_{ij} (N_{\rm ref})$  represents the distance between particles i and j after an affine deformation resulting from the application of a local strain  $\Lambda_i$  to the initial interparticle distance  $R_{ij} (N_{\rm ref})$ . This consists in computing the  $L^2$ -norm of the matrix multiplication between the local strain tensor  $\Lambda_i$  and the distance vector  $R_{ij} (N_{\rm ref})$  between particles i and j at the  $N_{\rm ref}$ th cycle:

$$\Lambda_{i}R_{ij}(N_{\text{ref}}) = \begin{bmatrix} \lambda_{xx} & \lambda_{xy} & \lambda_{xz} \\ \lambda_{yx} & \lambda_{yy} & \lambda_{yz} \\ \lambda_{zx} & \lambda_{zy} & \lambda_{zz} \end{bmatrix} \begin{bmatrix} r_{x} & r_{y} & r_{z} \end{bmatrix}^{T}_{2}$$
(3)

where  $\lambda_{xy}$  is the strain component of  $\Lambda_i$  in the xy-axis plane and  $r_x$  is the projection of the distance vector  $R_{ij}(N_{\rm ref})$  along the x-axis. The calculation of non-affine squared displacement  $D^2_{\rm min}$  is implemented by using the OVITO software [42].

### 2.5. Average energy barrier of the particles

To explore the topography of the potential energy landscape (PEL) of the initial static gel configuration (before any stress is applied), we adopt the activation-relaxation technique nouveau (ARTn) method [43]. Starting from a local minimum of PEL, the ARTn algorithm systematically searches for the saddle points and transition pathways that are accessible from this minimum. This allows us to compute the distribution of the energy barriers (i.e., difference of energy between the saddle point and the original local minimum) that are locally accessible to each particle. In detail, starting from the initial gel configuration (located in a local minimum of the PEL), the target particle and the first-coordination neighbors thereof are first activated with a random displacement so as to identify a direction of negative curvature that denotes the presence of a nearby saddle point within the energy landscape. The activated system is then relaxed toward the saddle point by following the direction of the negative energy curvature until the force is smaller than a given threshold (here, 0.04  $\varepsilon/\sigma$ ). The Lanczos algorithm is adopted to search for the saddle points. The step size during activation and relaxation are set as  $0.02\sigma$  and  $0.0004\sigma$ , respectively, and the curvature threshold to start relaxation is fixed at  $-1.0 \ \varepsilon/\sigma^2$  [43]. Finally, we compute the energy barrier associated with the target particle's rearrangement by subtracting the energy of the saddle point with the initial minimum energy. As such, the ARTn method restricts its search of particle rearrangements to those going through well-defined saddle points and, hence, focuses on the tiny fraction of the configurational space that is physically accessible to the system. To estimate the local distribution of energy barriers that are accessible to each particle, we conduct 20 independent saddle point searches for each particle- which is here found to be large enough to ensure the convergence of the energy barrier distribution [44]. Based on this analysis, we then compute the average value  $E_{ave}$  of the energy barriers that are accessible to each particle [45].

#### 3. Results

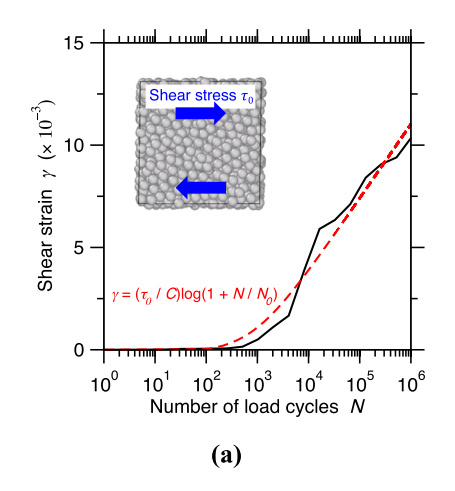
#### 3.1. Long-time creep dynamics

We adopt an accelerated simulation technique based on stress perturbations to simulate the long-time creep behavior of colloidal gels subjected to a sustained shear stress  $\tau_0$  [33,34]. Details regarding the creep simulation can be found in the Methods section and in Ref. [8]. Fig. 1a shows an example of shear strain  $\gamma$  evolution as a function of the number of stress perturbation cycles N. In agreement with previous works [8,9], our simulation predicts a logarithmic creep, which follows:

$$\gamma(N) = (\tau_0/C)\log(1 + N/N_0)$$
 (4)

where C, the creep modulus, is a material constant [8] and  $N_0$  is a fitting parameter that is analog to a typical relaxation time [2,8]. Importantly, the creep modulus obtained from this method was shown to match experimental data obtained on C–S–H gels—which confirms that the creep deformation induced by our accelerated method is similar to the one that would spontaneously occur over time [8].

Since the present simulation successfully reproduces the macroscopic creep of C-S-H gels, we now further analyze the simulated trajectories to explore the particle-scale mechanism of creep—which is typically hidden from conventional experiments [8,9].



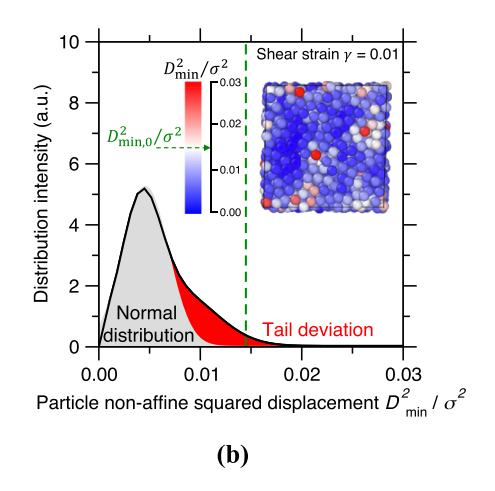


**Fig. 1.** (a) Shear strain  $\gamma$  as a function of the number of stress perturbation cycles of a colloidal C–S–H gel subjected to a constant shear stress  $\tau_0$ . The dashed line is a logarithmic fit following Eq. (4). (b) Distribution of the normalized non-affine squared displacement  $D^2_{\min}/\sigma^2$  for a shear strain  $\gamma=1$ %. The red area highlights the tail of the distribution, i.e., its deviation from a Gaussian distribution (in gray). The inset shows the corresponding gel configuration, wherein the color of the particles denotes their  $D^2_{\min}/\sigma^2$  value. The green dash line indicates the threshold ( $D^2_{\min}/\sigma^2$ ) that is used herein to discriminate immobile (low displacement) from mobile (high displacement) particles. (For interpretation of the references to color in this figure legend, the reader is referred to the web version of this article.)

To this end, we compute the normalized non-affine squared displacement  $D_{\min}^2/\sigma^2$  of each particle [22,41]—a metric that has been widely used to identify particle reorganizations under stress [12,46,47]. Details regarding the calculation of  $D_{\min}^2/\sigma^2$  can be found in the Methods section. Fig. 1b shows the distribution of the  $D_{\min}^2/\sigma^2$  values for a shear strain  $\gamma=1\%$ . We observe that the distribution is centered around a low displacement value (i.e.,  $D_{\text{min}}^2/\sigma^2 = 0.005$ ), which corresponds to the population of particles that do not exhibit significant reorganizations upon creep. However, we note that the distribution also exhibits a long tail toward large displacement values, suggesting that a few select particles feature some significant reorganizations. In the following, we use a threshold normalized non-affine squared displacement of  $D^2_{\min,0}/\sigma^2 = 0.014$  (corresponding to a displacement of about 12% of  $\sigma$ ) to classify particles as immobile (low displacement) or mobile (high displacement). Based on this threshold, about 7% of the particles are classified as mobile during the creep process. Note, however, that the following analysis does not significantly depend on the arbitrary choice of this threshold displacement (see Supplementary Materials).

#### 3.2. Particle mobility classification by machine learning

We now investigate whether the propensity of a particle to be mobile or immobile (i.e., a dynamic property) could in some ways be encoded in its static initial structure (before loading). To this end, following the example of the softness approach [12,22], we construct by machine learning a structural quantity that is correlated to the propensity of a particle to exhibit a local rearrangement upon creep deformation. Each step of the machine learning pipeline is explained in detail in the Supplementary Materials. Briefly, we first construct a dataset composed of ~17,000 particles obtained from 10 independent creep simulations (with 10 distinct initial configurations). Each system exhibits a similar distribution of  $D^2_{\min}/\sigma^2$  at the end of creep simulation. From this dataset, 7 configurations serve as training set, while the remaining 3 configurations are used as test set. Each particle is classified as mobile  $(D^2_{\min}/\sigma^2 \geq D^2_{\min,0}/\sigma^2)$  or immobile  $(D^2_{\min}/\sigma^2 < D^2_{\min,0}/\sigma^2)$  based on its final normalized non-affine squared displacement (at the end of the creep simulation). We then calculate a series of structural features for each particle based on the initial static structure (before any stress is applied). In detail, we calculate for each particle i a series of  $N_r$  radial order parameters G(i; r)associated with different distances r:

$$G(i;r) = \sum_{i} e^{-(R_{ij}-r)^{2}/L^{2}}$$
 (5)

where j refers to the neighbor particles of i within a cutoff distance  $R_G$  (here,  $R_G = 6\sigma$  [22]),  $R_{ij}$  is the distance between the particles i and j, and L is the standard deviation of the Gaussian functions centered around r (here,  $L = 0.04\sigma$  [22]). In short, this metric is related to the local density of neighbors at a distance r from the central particle i, as averaged over a shell with a typical thickness L. We calculate for each particle i these  $N_r$  order parameters for varying r distances (ranging from  $0.6\sigma$  to  $3\sigma$  with an increment of  $0.04\sigma$  [22]). All these features are standardized prior to any training [48]. Altogether, the ensemble of these metrics offers an unbiased fingerprint of the local radial order around each individual particle. We then train a classifier to identify the optimal hyperplane separating mobile from immobile particles within the  $N_r$ -dimensional space associated with the values of the  $N_r$  radial order parameters.

In contrast to the original softness approach that uses both radial and angular order parameters as input features [12,22], we solely focus on features capturing radial 2-body correlations around each particle. This is key to ensure that the new softness

metric remains highly interpretable (see Section 4.1). Note that, since the particles are monodisperse and do not exhibit any bond directionality, the incorporation of angular 3-body order parameters does not notably increase the accuracy of the classification model (see Supplementary Materials for details). In that regard, limiting the number of input features also allows us to ensure that the model does not become overfitted. Moreover, unlike the original softness approach based on the Support Vector Machine (SVM) classifier [12,22], we adopt logistic regression to build the classifier [48]. This classifying technique offers great model simplicity, accuracy, and interpretability (see Supplementary Materials for details). Indeed, logistic regression directly provides the probability of a given particle to be mobile or immobile. In addition, it embeds regularization to limit the risk of overfitting. Importantly, the classification hyperplane determined by logistic regression is linear, which makes it possible to easily assess the importance of each feature. We also expect that the linear nature of the hyperplane is key to enhance the extrapolability of the classification model.

Fig. 2a illustrates the outcome of the classification, where we select as horizonal and vertical axis the two most influential features of the classification model (see Section 4.1) in order to illustrate a two-dimensional projection of the positions of the particles in the  $N_r$ -dimensional feature space. Each particle is then colored based on its relative non-affine squared displacement. Finally, Fig. 2a shows the hyperplane identified by logistic regression, which effectively discriminates mobile from immobile particles. Notably, we find that, based on the knowledge of the structural features, this classifier properly classifies particles as mobile or immobile with an accuracy of 75% and 70% for the training and test sets, respectively (see Supplementary Materials for details). Interestingly, this signals that the propensity for particles to dynamically rearrange during the long-time creep of the gel is largely encoded in its initial static structure (before any stress is applied).

# 3.3. Machine-learned structural metric governing particles' dynamics

The softness S of each particle is then defined as the orthogonal distance from the hyperplane to its position in the  $N_r$ -dimensional feature space, wherein mobile (soft) and immobile (hard) particles are associated with positive and negative values of S, respectively. Fig. 2b shows the distribution density of the particles' normalized non-affine squared displacement  $D^2_{\min}/\sigma^2$  (at the end of the creep simulation) and their initial softness S (at the beginning of the simulation, before any stress is applied). We find that, based on the softness sign (S > 0 or S < 0), the mobile particles  $(D^2_{\min}/\sigma^2 \ge D^2_{\min,0}/\sigma^2)$  can be well discriminated from the immobile particle  $(D^2_{\min}/\sigma^2 < D^2_{\min,0}/\sigma^2)$ . Further, Fig. 2c shows the final average normalized non-affine squared displacement  $\langle D^2_{\min}/\sigma^2 \rangle$  of the particles as a function of their softness S, both for the training and test sets. We find that the normalized non-affine squared displacement of the particles features a power-law dependence on softness. Namely, in addition of properly discriminating mobile from immobile particles, the softness metric also offers some information on the magnitude of the displacement-that is, the particles that exhibit the largest reorganization upon creep are associated with the largest softness values, and vice versa. This power-law correlation is likely to be rooted in the fact the particle dynamics is encoded in the topography of energy landscape of the initial static gel structure (see Section 4.3).

Notably, the degree of correlation between softness and particle dynamics during creep remains high for particles belonging to the test set. Fig. 3a offers a snapshot of the predicted softness of an initial static gel configuration in the test set. The distribution of softness (both for all particles and for mobile particles in the gel) is provided in Fig. 3b. We find that the classification accuracy is satisfactory as ~76% of the mobile particles indeed exhibit a posi-

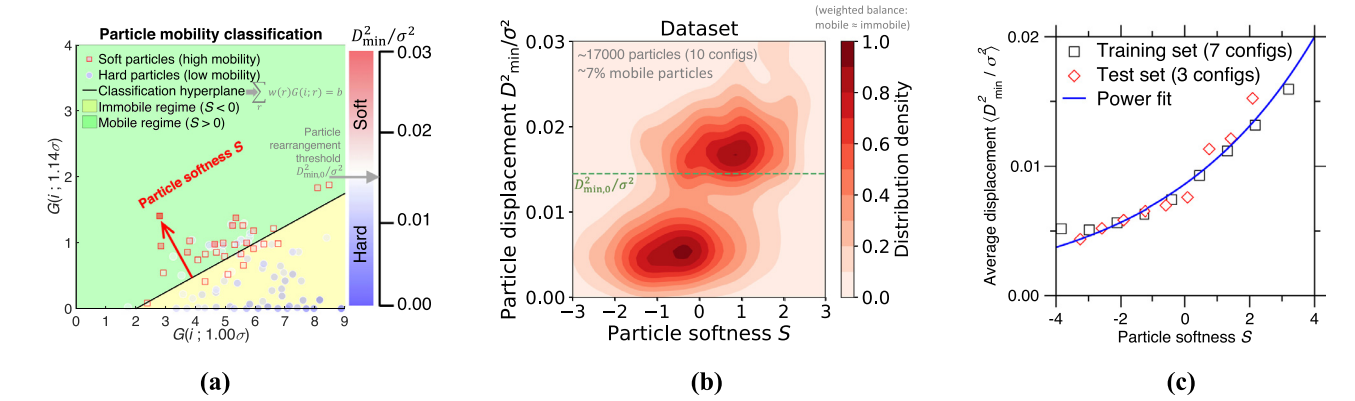
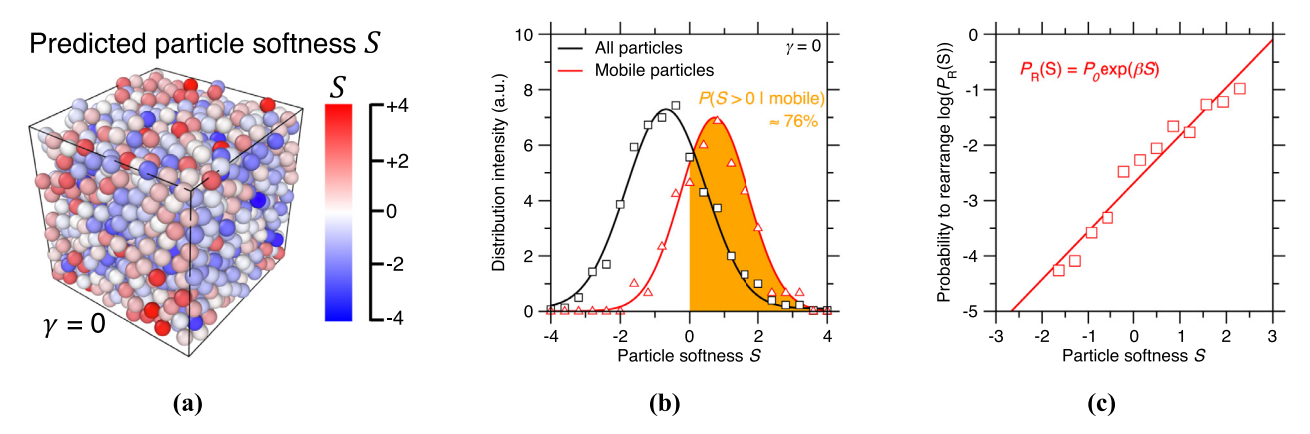


Fig. 2. (a) Illustration of the classifier model, wherein the position of each particle is determined from the values of the two most influential structural features used for the classification, i.e., the order parameters G(i; r) calculated at  $r_0 = 1.00\sigma$  and  $r_1 = 1.14\sigma$ . The color of each particle denotes its relative non-affine squared displacement  $(D^2_{\min}/\sigma^2)$ . The black line represents the projection of the hyperplane identified by logistic regression in this 2-dimensional space. (b) Distribution density of the particles' normalized non-affine square displacement  $(D^2_{\min}/\sigma^2)$  (at the end of the creep simulation) and initial softness (S), wherein the softness of each particle is defined as the orthogonal distance from the hyperplane to its position in the  $N_r$ -dimensional feature space (see panel a). The dataset consists of 10 creep simulations (~1700 particles and ~7% mobile particles per configuration), wherein 7 final configurations serve as training set and the rest 3 configurations are test set. The green dash line indicates the threshold  $(D^2_{\min,0}/\sigma^2)$  of particle rearrangement. For illustration purposes, the density of mobile particles is rescaled to ensure balance with the number of immobile particles. (c) Final average normalized non-affine squared displacement  $\langle D^2_{\min}/\sigma^2 \rangle$  of the particles of the training and test sets (at the end of the creep simulation) as a function of their initial softness. The blue line is a power fit to guide the eye. (For interpretation of the references to color in this figure legend, the reader is referred to the web version of this article.)



**Fig. 3.** (a) Snapshot of the predicted particles' softness of an initial static gel (shear strain  $\gamma=0$ ) in the test set. (b) Distribution of the softness of all particles (black) and mobile particles (red) in the gel. The orange area represents the fraction of properly predicted soft particles (S>0) within the mobile particles. (c) Logarithm of the probability of a particle to rearrange upon creep  $(D^2_{\min}/\sigma^2 \ge D^2_{\min,0}/\sigma^2) \log(P_R(S))$  as a function of its initial softness S in the initial gel structure. The red line is an exponential fit following Eq. (6). (For interpretation of the references to color in this figure legend, the reader is referred to the web version of this article.)

tive softness (S > 0). We then calculate the probability of a particle to rearrange  $P_R(S)$  as a function of its initial softness S in the gel (see Fig. 3c). Interestingly, we find that  $P_R(S)$  exhibits an exponential dependance on the softness metric S, wherein the larger the softness is, the more likely the particle is to rearrange. This relationship can be formulated in terms of the behavior of an activated process in Eq. (6) [49]:

$$P_{R}(S) = P_{0}\exp(\beta S) \tag{6}$$

where  $P_0$  and  $\beta$  are some fitting parameters. This exponential relationship between  $P_R(S)$  and S suggests that the structural quantity S is closely related to (and might be indicative of) the energy barrier associated with particle rearrangements [23,26] (see Section 4.4). Note that softness is calculated based on the sole knowledge of the initial structure, whereas the normalized nonaffine squared displacement is computed at the end of the simulation (i.e., after the gel has creeped to exhibit a shear strain of about 1%). The high degree of correlation between initial softness and final normalized non-affine squared displacement clearly illustrates the intimate link between the initial static structure of the gel and its long-time creep dynamics.

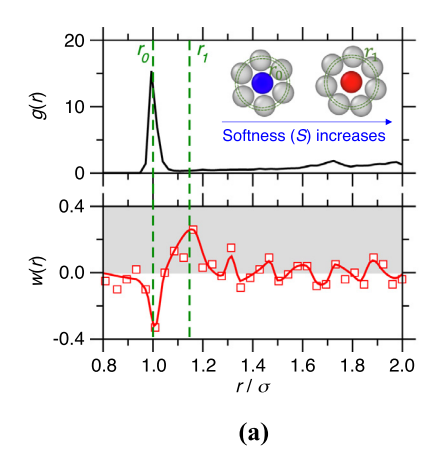
#### 4. Discussion

### 4.1. Structural interpretation of "particle softness"

We now discuss the structural interpretation of the machine-learned softness metric. As a key advantage of our approach, using the radial order parameters G(i; r) as sole features of the classifier and adopting logistic regression make the softness metric that is constructed herein highly interpretable. Indeed, the hyperplane created by logistic regression can be expressed as a linear equation of each of the features as (see Fig. 2a):

$$\sum_{r} w(r)G(i;r) = b \tag{7}$$

wherein w(r) and b are the coefficients and the bias of the logistic regression model, respectively. Since the features G(i; r) are standardized, the coefficients are directly indicative of the relative importance of each feature in the classification. Namely, a large absolute value for w(r) denotes that the hyperplane is fairly orthogonal to the axis associated with the corresponding feature G(i; r). In addition, the sign of the coefficients is informative, since positive and negative values for w(r) indicate that increasing values of the



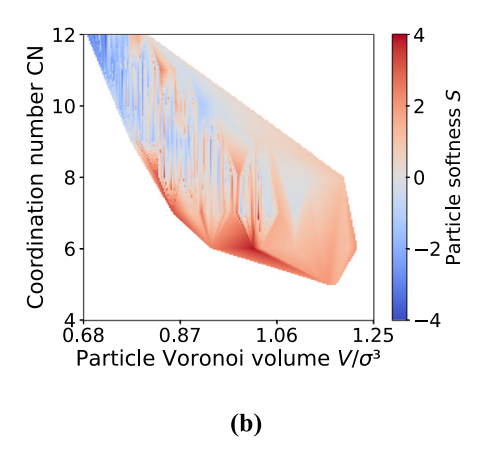


**Fig. 4.** (a) Weight coefficient w(r) of classification hyperplane (see Fig. 2(a)) at different normalized distances  $r/\sigma$ . The red line is to guide the eyes. The pair distribution function g(r) of the gel is added in the top panel as reference. The distances  $r_0 = 1.00\sigma$  and  $r_1 = 1.14\sigma$  are associated with the most influential input features of the classifier, i.e., the w(r) coefficients showing maximum absolute value. The inset illustrates the local environments around (i) "hard" particles (blue), wherein the neighbors are located at  $r_0 = 1.00\sigma$  and (ii) "soft" particles (red), wherein the neighbors are located at  $r_1 = 1.14\sigma$ . (b) Particle softness S as a function of their normalized particle Voronoi volume  $V/\sigma^3$  and coordination number CN. The color coding is based on a linear interpolation between the datapoints in the particle dataset. (For interpretation of the references to color in this figure legend, the reader is referred to the web version of this article.)

feature G(i; r) tend to result in increased and decreased softness values, respectively.

Fig. 4a shows the coefficients w(r) of the logistic regression classifier as a function of the distance r, wherein the absolute value of w(r) denotes how influential the feature G(i; r) is. We find that the two most influential features are associated with the distances  $r_0 = \sigma$  and  $r_1 = 1.14\sigma$ . A visual inspection of the pair distribution function of the gel (see the upper panel of Fig. 4a) reveals that  $r_0$  represents the average interparticle bond distance (i.e., equilibrium position of particle interaction energy), while  $r_1$  represents a distance between the 1st and the 2nd coordination shells. This indicates that the local density of neighbors centered around these distances plays a critical role in discriminating mobile from immobile particles. On the one hand, the local density of atoms at  $r=r_0$  is related to the coordination number (CN) of the central particle when the neighbors are in contact with the central particle (see blue particle in Fig. 4a). The fact that  $w(r_0) < 0$  indicates that large CNs tend to result in lower softness values. On the other hand, we interpret the distance  $r_1$  as that wherein neighbors are located when there is coordination mismatch around the central particle (e.g., an excess of neighbors, see red particle in Fig. 4a). The fact that  $w(r_1) > 0$  indicates that the presence of such coordination mismatch tends to result in higher softness values. These results are consistent with free volume theory (FVT) [8,9]. Indeed, closed-packed structures with a large number of atoms at  $r = r_0$ are associated with low local free volume, wherein the atoms exhibit very limited mobility. In contrast, more disordered structures exhibiting notable coordination mismatch tend to show larger local free volume (see red particle in Fig. 4a), which facilitates particle mobility.

The absolute values of the coefficients w(r) associated with other distances are notably lower and, hence, the local density of neighbors at such distance has a smaller influence on the outcome of the classification. The features associated with these other distances are nevertheless important for the accuracy of the classifier. Indeed, we find that, even though our results suggest that the local free volume plays an important role in creep dynamics, the classification model trained based on the sole knowledge of the particle Voronoi volume offers a limited accuracy of ~60% as compared to that offered by the softness metric (~75% accuracy, see Supplementary Materials for details). Fig. 4b illustrates the dependence of softness on the particles' coordination number CN and Voronoi volume V. Overall, larger CN and smaller V values tend

to favor smaller softness. However, we nevertheless observe that softness is a complex, nonmonotonic function of CN and V. We note that training a classifier based on the sole knowledge of the particles' CN only yields an accuracy of ~55%, wherein both low and high-coordination particles are very likely to be classified as soft particles (see Supplementary Materials for details), so that the soft vs. hard nature of particles cannot simply be inferred based on Maxwell criterion on stability [50,51]. Similarly, only using  $G(i; r_0)$  and  $G(i; r_1)$  as input features yields a very limited accuracy of ~50%. This exemplifies the benefit of using an unbiased machine learning approach to build the set of input features, since intuitive structural features show only limited correlation with dynamical properties.

# 4.2. Linking particle dynamics to macroscopic deformation

We now look into the nature of the relationship between particle-level softness (see Fig. 3c) and the macroscopic creep of the gel (see Fig. 1a). To this end, we consider the average softness  $\langle S \rangle$  of the system—i.e., as averaged over all the particles—and assess how this quantity is evolving as the gel gradually undergoes creep (see the inset of Fig. 5). We find that  $\langle S \rangle$  exhibits a logarithmic decay upon creep, which echoes the logarithmic increase of the macroscopic strain of the gel upon creep (see Fig. 1a). In fact, as shown in Fig. 5, we observe that the macroscopic creep rate  $\dot{\gamma}$  of the gel exhibits an exponential dependence on  $\langle S \rangle$  as:

$$\dot{\gamma} = \dot{\gamma}_0 \exp(\alpha \langle S \rangle) \tag{8}$$

where  $\dot{\gamma}_0$  and  $\alpha$  are some fitting parameters. Note that this exponential relationship is not affected by the system size (see Supplementary Materials for details). This indicates that the dynamics of creep at the macroscopic scale is closely related to the variation in softness at the particle level. This can be understood as follows. The gradual decay of softness indicates that, upon creep, particles reorganize from "soft" (i.e., high S) to "harder" (i.e., lower S) local environments (see the schematics in Fig. 4a). In turn, as the softness of a particle decreases, so does its propensity to exhibit any further reorganization. This process explains why the creep rate gradually slows down—since the particles gradually become harder and harder and, hence, less prone to reorganizations. It is worthwhile to point out that, although our softness results illustrate a strong correlation between the initial static structure and the early-stage creep dynamics, it remains unclear whether

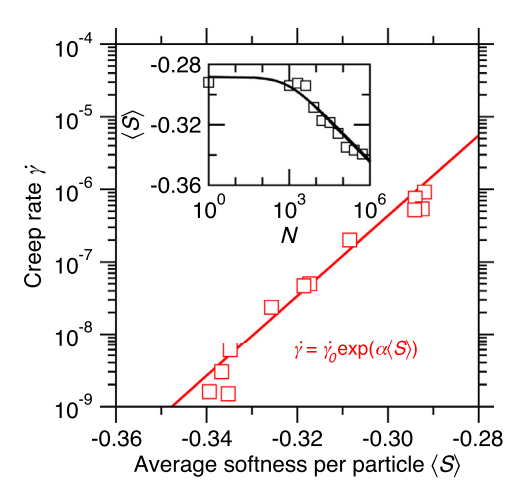


**Fig. 5.** Macroscopic creep rate  $\dot{\gamma}$  of the gel as a function of the average softness  $\langle S \rangle$  of the particles. The red line is an exponential fit following Eq. (8). The inset shows the evolution of  $\langle S \rangle$  in the gel upon creep. (For interpretation of the references to color in this figure legend, the reader is referred to the web version of this article.)

the softness approach presented herein could describe longer-term effects (e.g., final avalanche) based on the static initial structure since the system tends to lose the memory of its initial configuration after experiencing significant deformations [11,39,40,52]. Here, the exponential dependence of the creep rate on the average softness is a macroscopic manifestation of the particle-level exponential dependence of particle dynamics on its softness in Eq. (6) (see Fig. 3c), which suggests that  $\langle S \rangle$  (or, more accurately, the opposite thereof) captures an effective average energy barrier for creep [2,8]—wherein low  $\langle S \rangle$  values (i.e., "hard" structures) are indicative of high energy barriers for particle rearrangements, and vice versa (see below) [23,26].

#### 4.3. The energy landscape governs the particle dynamics during creep

Since the results shown in Fig. 5 suggest that softness may be capturing the effective energy barrier that is accessible to the particles during creep, we now further investigate the linkage between creep dynamics and potential energy landscape (PEL) topography [49]. Fig. 6a offers a schematic of the local PEL that is accessible to an initial static gel (before any stress is applied). The initial configuration is located at a local minimum of the PEL. Starting from this initial position, the ARTn algorithm searches for saddle points around the local minimum, which are associated with physically-meaningful rearrangements for a target particle [43]. This allows us to compute the distribution of the energy barriers that are locally accessible to each particle (i.e., the energy difference between the identified saddle point and initial minimum, see Section 2.5). Based on this analysis, we then calculate, for each particle, the average value  $E_{ave}$  of the energy barriers that are accessible to this particle.

Fig. 6b shows the distribution of the normalized average energy barrier  $E_{\rm ave}/\varepsilon$  of the particles in the initial static gel. We find that the distribution decreases with increasing energy barrier value and exhibits a long tail toward high energy barriers. Fig. 6c shows the distribution density of the particles' normalized non-affine squared displacement  $D^2_{\rm min}/\sigma^2$  (at the end of the creep simulation) and initial normalized average energy barrier  $E_{\rm ave}/\varepsilon$ . We observe the existence of an anticorrelation between displacement and average energy barrier—which is a natural consequence of the fact that particles that are surrounded only by large energy barriers (i.e., rough local energy landscape) are trapped around their local minimum and unable to reorganize [49]. However, for low  $E_{\rm ave}/\varepsilon$  values, we find that only a small fraction of the particles tends to exhibit a

large displacement (i.e., to be mobile). This can be explained based on the spatial heterogeneity of the  $D^2_{\rm min}/\sigma^2$  and  $E_{\rm ave}/\varepsilon$  fields in the gel (see discussion on the point in Section 4.4).

Fig. 6d shows the final average normalized non-affine squared displacement  $\langle D^2_{\min}/\sigma^2 \rangle$  of the particles in the gel (at the end of the creep simulation) as a function of their normalized average energy barrier  $E_{\text{ave}}/\varepsilon$  (in the initial configuration, before any stress is applied). Interestingly, we find the existence of a power-law relationship between  $\langle D^2_{\min}/\sigma^2 \rangle$  and  $E_{\text{ave}}/\varepsilon$ , wherein larger  $E_{\text{ave}}/\varepsilon$  tend to result in smaller  $D_{\min}^2/\sigma^2$  values, and vice versa (see Fig. 6d). This result echoes the power-law relationship between  $\langle D^2_{\min}/\sigma^2 \rangle$ and softness S previously highlighted in Fig. 2c. The harmony between these trends suggests the existence of a potential causal relationship between softness S and average energy barrier  $E_{ave}$  (see Section 4.4). In addition, these results also echo findings from a recent study, which reported the existence of a power-law relationship between particle dynamics and energy barrier in metallic glasses [44,45]. This suggests that this power-law relationship between particle dynamics and energy barrier (or particle softness) might be a generic feature of disordered systems, independently of whether the particle reorganizations are caused by creep or not.

Finally, we evaluate the probability of a particle to rearrange  $P_R(E_{\text{ave}})$  as a function of its initial average energy barrier  $E_{\text{ave}}$  (see Fig. 6e). We find  $P_R(E_{\text{ave}})$  follows an exponential dependence on  $E_{\text{ave}}$  that echoes that of an activated process [49]:

$$P_R(E_{\text{ave}}) = P_E \exp\left(-\beta_E E_{\text{ave}}\right) \tag{9}$$

where  $P_E$  and  $\beta_E$  are some fitting parameters. Namely, the larger the average energy barrier is, the less likely the particle is to reorganize. Overall, these results indicate that the dynamics of a gel upon creep is largely encoded in the topography of its initial energy landscape, before any load is applied. The harmony between Eqs. (6) and (9)—which can both be described in terms of an activated process—suggests a strong correlation between the softness S and average energy barrier  $E_{\rm ave}$  fields (see below).

# 4.4. Mapping "particle softness" to energy barrier

Finally, we interrogate the existence of a causal correlation between softness S and average energy barrier  $E_{\rm ave}$ . Fig. 7a illustrates the spatial correlation between the fields of interest herein: (i) the final non-affine squared displacement ( $D^2_{\rm min}$ ), (ii) the initial softness (S), and (iii) the initial average energy barrier ( $E_{\rm ave}$ ). We find that the three fields—i.e., the dynamics field ( $D^2_{\rm min}$ ), the structural field (S), and the local potential energy landscape field ( $E_{\rm ave}$ )—all show a strong degree of spatial heterogeneity, but are fairly correlated to each other. Namely, the regions associated with low mobility tend to match with those presenting high energy barriers and low softness, and vice versa.

Fig. 7b shows the distribution density of the particles' initial normalized average energy barrier  $(E_{\text{ave}}/\varepsilon)$  and initial softness (S). Overall, we observe that the particles associated high softness values (i.e., "soft" mobile particles, S>0) tend to exhibit fairly low average energy barriers. However, we note that the correlation between softness and average energy barriers is not as strong as that observed between softness and displacement, or energy barriers and displacement (see Figs. 2b and 6c). Nevertheless, a stronger correlation between softness and energy landscape emerges when averaging these fields over groups of particles featuring fairly similar softness. To this end, Fig. 7c shows the initial average normalized energy barrier  $\langle E_{\text{ave}}/\varepsilon \rangle$  of the particles in the gel (before any stress is applied) as a function of their initial softness S. Interestingly, we find that  $\langle E_{\text{ave}}/\varepsilon \rangle$  is linearly related to the opposite of softness (-S, or "hardness" H) as:

$$E_{\text{ave}}(H) = kH + b \tag{10}$$

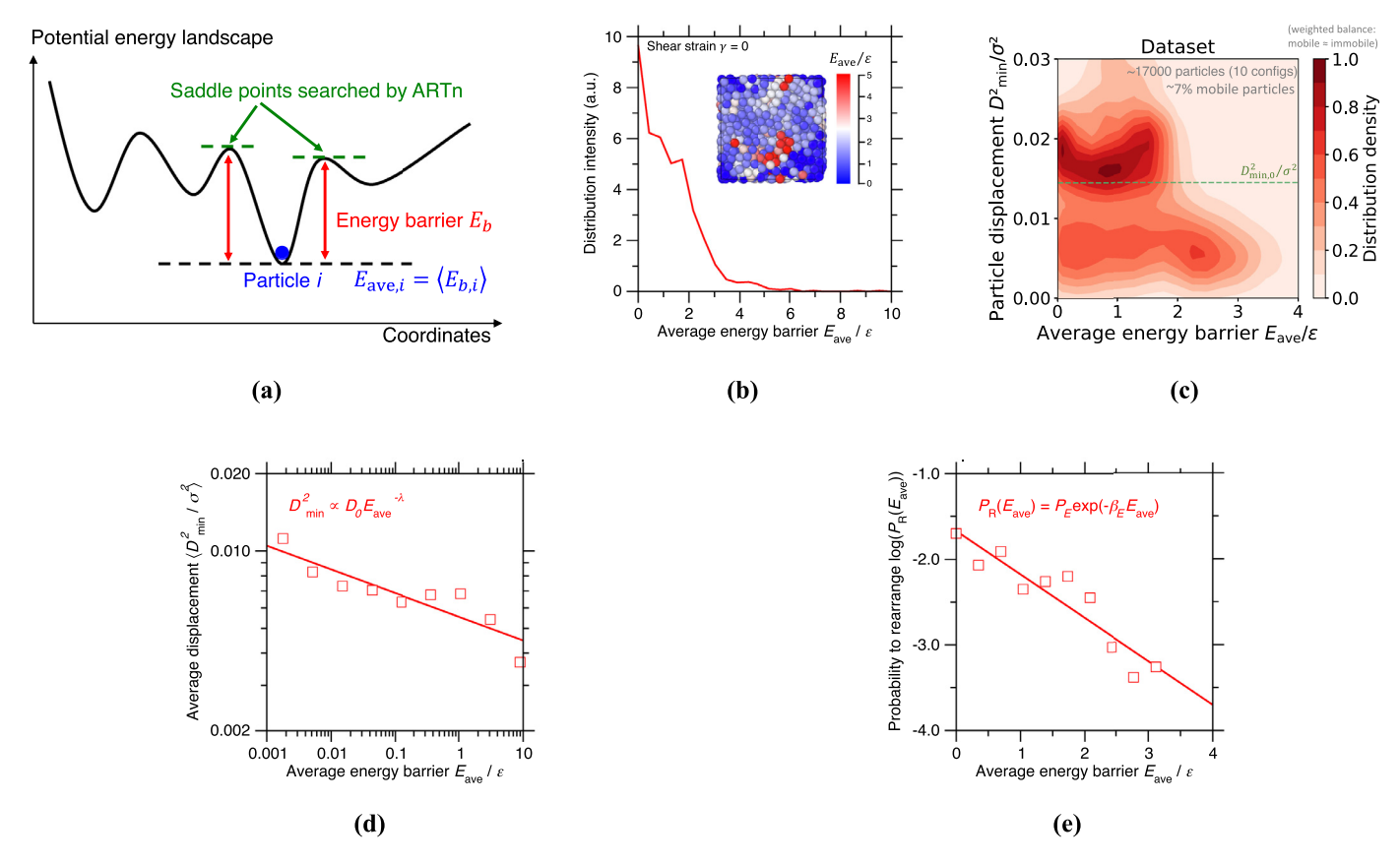


Fig. 6. (a) Schematic illustrating the local potential energy landscape (PEL) of an initial static gel. The gel is initially located at a local minimum of the PEL. Starting from this minimum position, the activation-relaxation nouveau (ARTn) algorithm searches the saddle points that are locally accessible to target particles [43] (see Methods section for details).  $E_{ave}$  is the average value of the energy barriers that are accessible to a given particle. (b) Distribution of the normalized average energy barrier  $E_{ave}/\varepsilon$  of the particles in the initial static gel (before any stress is applied). The inset shows the associated gel configuration, wherein the color of the particles denotes  $E_{ave}/\varepsilon$ . (c) Distribution density of the particles' normalized non-affine square displacement  $(D^2_{min}/\sigma^2)$  (at the end of the creep simulation) and initial normalized average energy barrier  $(E_{ave}/\varepsilon)$ . (d) Final average normalized non-affine squared displacement  $(D^2_{min}/\sigma^2)$  of the particles in the gel (at the end of the creep simulation) as a function of their initial normalized average energy barrier  $(E_{ave}/\varepsilon)$ . The red line is a power-law fit. (e) Logarithm of the probability of a particle to rearrange upon creep  $(D^2_{min}/\sigma^2 \geq D^2_{min,0}/\sigma^2)$  log( $P_R(E_{ave})$ ) as a function of its initial normalized average energy barrier  $E_{ave}/\varepsilon$  in the gel. The red line is an exponential fit following Eq. (9). (For interpretation of the references to color in this figure legend, the reader is referred to the web version of this article.)

where k and b are some fitting parameters. This shows that the topography of the energy landscape is largely encoded in the structure of the gel. Importantly, these results demonstrate that, when averaged over groups of particles, the average softness indeed offers a purely structural metric that successfully captures the average height of the energy barriers that are locally accessible, which, in turn, controls the particles' propensity to reorganize upon creep [23,26]. It is notable that the softness metric is able to successfully capture a structural fingerprint for the topography of the potential energy landscape since this machine-learned quantity is not trained for that purpose (that is, the model is never exposed to the energy barriers during its training). As such, the correlation between softness and average energy barrier offers an independent validation of the soundness of this approach-and suggests that the softness metric that is extracted herein indeed shows a "real" physical meaning.

Note that, in this analogy between softness and energy barriers, the energy barriers that are captured by softness are not overcome by thermal effects, but by the applied stress—which provides an elastic energy that enables particles to jump over these barriers [2,8]. An interesting atomic picture behind the link between energy landscape topography, applied external stress (or strain), and resulting particle hoping is offered by the trap model—which describes the energy landscape as a landscape of "traps," wherein an external stress can facilitate particle hopping from trap to trap by deforming the local landscape [49]. In that regard, our results sug-

gest that softness might serve as a proxy for the average height of the energy barriers that separate the traps within the energy landscape

To further explore the degree of spatial heterogeneity in the three fields considered herein, we compute the spatial correlation function  $\langle C(0)C(r)\rangle$  for each field (see Fig. 7d), where C(r) is the normalized fluctuation in the field, i.e., the standardized field value  $(D^2_{\min}, S, \text{ and } E_{\text{ave}})$  of a particle at distance r from a central particle. The spatial correlation function  $\langle C(0)C(r)\rangle$  is computed by averaging over all particles separated by a distance r. We then infer the characteristic correlation length  $\xi$  associated with each field by fitting the spatial correlation function as [24]:

$$\langle \mathsf{C}(0)\mathsf{C}(r)\rangle = \mathsf{C}_0 \exp(-r/\xi) \tag{11}$$

where  $C_0$  is a fitting coefficient. We find that both the softness field and the energy barrier field show a similar correlation length  $\xi$  that is close to 1 (i.e., the typical radius of the first coordination shell). This harmony further supports the close relationship between softness and energy barriers. In contrast, the dynamics field shows a correlation length of  $\xi \approx 0.5$  (i.e., the typical radius of a particle). This indicates that the typical lengthscale associated with particle displacements is notably lower as compared to that associated with the softness/energy barriers fields. The fact that the lengthscale associated with displacements is lower than that of the energy barrier field likely explains why only a small fraction of the particles showing low  $E_{\rm ave}/\varepsilon$  values also feature large

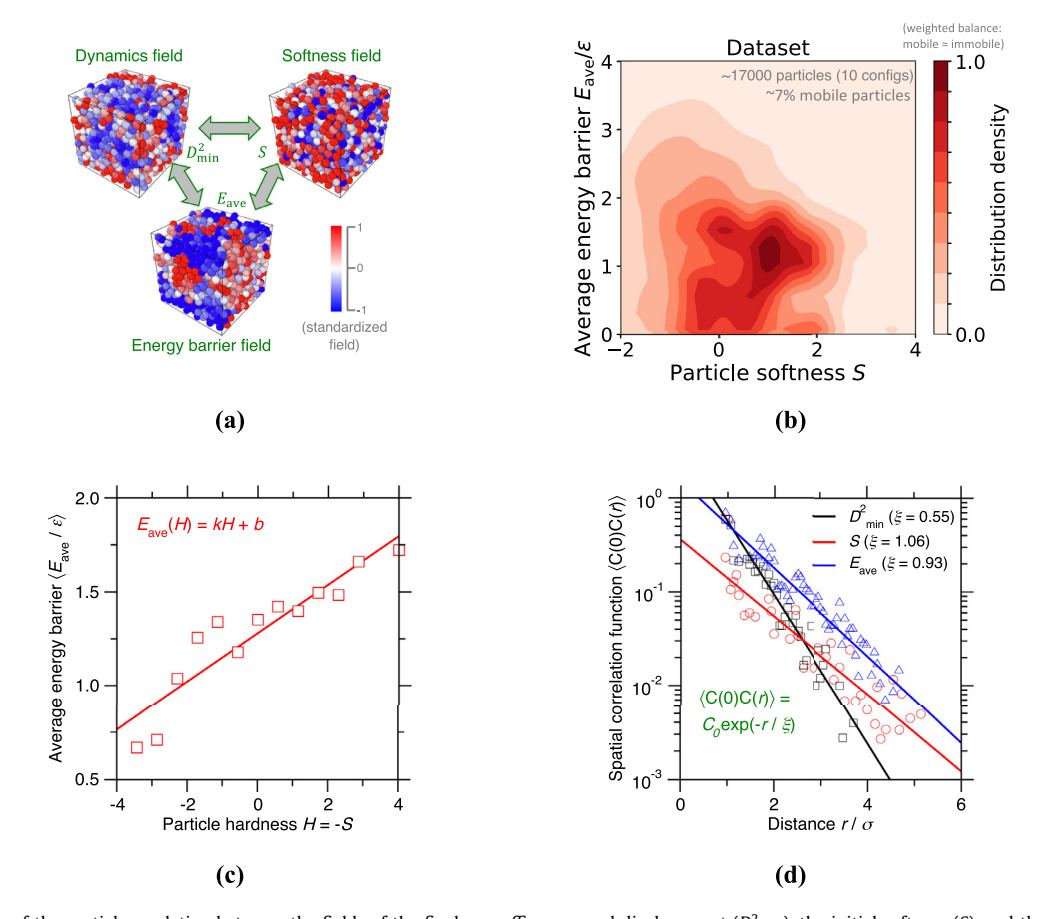


**Fig. 7.** (a) Illustration of the spatial correlation between the fields of the final non-affine squared displacement  $(D^2_{\min})$ , the initial softness (S), and the initial average energy barrier  $(E_{\text{ave}})$ . The particles are colored based on their standardized value in the corresponding field. (b) Distribution density of the particles' initial normalized average energy barrier  $(E_{\text{ave}}|\varepsilon)$  and initial softness (S). (c) Initial average normalized energy barrier  $((E_{\text{ave}}|\varepsilon))$  of the particles in the gel (before any stress is applied) as a function of their initial hardness (H = -S). The red line is a linear fit following Eq. (10). (d) Spatial correlation function (C(0)C(r)) of the displacement field  $(D^2_{\min})$ . black), the softness field (S, red), and the energy barrier field  $(E_{\text{ave}})$ , blue) in the gel. Note that the field value  $(C, P^2_{\min})$ ,  $(S, P^2_{\max})$  is standardized for the calculation. The lines are exponential fits following exp $(-r/\xi)$ , where  $\xi$  is the characteristic correlation length. (For interpretation of the references to color in this figure legend, the reader is referred to the web version of this article.)

displacements (see Fig. 6c). This partial decorrelation between the spatial distributions of displacement and energy barriers (or softness) may be a consequence of the fact that, here, displacement is induced by stress rather than being fully spontaneous. Consequently, "soft" particles that have access to low energy barriers may nevertheless not exhibit any notable displacement if the direction of the imposed stress does not match with any of the accessible low-energy saddle point pathways.

# Conclusions

Overall, these results highlight the close correlation between (i) static structure (as captured by softness), (ii) static potential energy landscape topography (as captured by the average height of the energy barriers that are accessible to the particles), (iii) particle dynamics (as captured by the non-affine squared displacement), and (iv) macroscopic deformation (as captured by the creep rate). It is notable that our approach allows us to predict the longtime dynamics of the particles upon long-term creep deformations while solely relying on the knowledge of the initial static structure before any stress is applied. The accessible interpretation of the softness metric defined herein (see Fig. 4a) suggests that the degree of structural disorder-and especially the existence of coordination mismatches-plays a key role in governing the creep dynamics of gels. This indicates that order-disorder engineering of gel structures offers a potential path to develop new gel formulations with tailored creep response under sustained load.

#### **Declaration of Competing Interest**

The authors declare that they have no known competing financial interests or personal relationships that could have appeared to influence the work reported in this paper.

# Data availability

All data needed to evaluate the conclusions in the paper are present in the paper and/or the Supplementary Materials. Additional data related to this paper may be requested from the authors.

# Acknowledgments

This work is supported by the National Science Foundation under Grants No. CMMI-1562066, DMR-1944510, and DMREF-1922167, as well as the International Cooperation on Scientific and Technological Innovation Programs of BGRIMM under Grant No. 2017YFE0107000.

#### Supplementary materials

Supplementary material associated with this article can be found, in the online version, at doi:10.1016/j.actamat.2021.116817.

#### References

- V.B. Nguyen, T. Darnige, A. Bruand, E. Clement, Creep and fluidity of a real granular packing near jamming, Phys. Rev. Lett. (2011) 107, doi:10.1103/ PhysRevLett.107.138303.
- [2] M. Bauchy, M. Wang, Y. Yu, B. Wang, N.M.A. Krishnan, E. Masoero, F.-J. Ulm, R. Pellenq, Topological control on the structural relaxation of atomic networks under stress, Phys. Rev. Lett. (2017) 119. doi:10.1103/PhysRevLett.119.035502.
- [3] M. Siebenbürger, M. Ballauff, Th. Voigtmann, Creep in colloidal glasses, Phys. Rev. Lett. (2012) 108, doi:10.1103/PhysRevLett.108.255701.
- [4] J.-P. Poirier, Creep of Crystals: High-Temperature Deformation Processes in Metals, Ceramics and Minerals, Cambridge University Press, 1985.
- [5] W.N. Findley, F.A. Davis, Creep and Relaxation of Nonlinear Viscoelastic Materials. Courier Corporation. 2013.
- [6] Y.M. Joshi, Dynamics of colloidal glasses and gels, Annu. Rev. Chem. Biomol. Eng. 5 (2014) 181–202, doi:10.1146/annurev-chembioeng-060713-040230.
- [7] M. Vandamme, F.-J. Ulm, Nanoindentation investigation of creep properties of calcium silicate hydrates, Cement Concr. Res. 52 (2013) 38–52, doi:10.1016/j. cemconres 2013 05 006
- [8] H. Liu, S. Dong, L. Tang, N.M. Anoop Krishnan, E. Masoero, G. Sant, M. Bauchy, Long-term creep deformations in colloidal calcium-silicate-hydrate gels by accelerated aging simulations, J. Colloid Interface Sci. 542 (2019) 339–346, doi:10.1016/j.jcis.2019.02.022.
- [9] M. Vandamme, F.-J. Ulm, Nanogranular origin of concrete creep, Proc. Natl Acad. Sci. 106 (2009) 10552–10557, doi:10.1073/pnas.0901033106.
- [10] K. Ioannidou, K.J. Krakowiak, M. Bauchy, C.G. Hoover, E. Masoero, S. Yip, F.-J. Ulm, P. Levitz, R.J.-M. Pellenq, E.D. Gado, Mesoscale texture of cement hydrates, Proc. Natl Acad. Sci. 113 (2016) 2029–2034, doi:10.1073/pnas. 1520487113.
- [11] V. Bapst, T. Keck, A. Grabska-Barwińska, C. Donner, E.D. Cubuk, S.S. Schoenholz, A. Obika, A.W.R. Nelson, T. Back, D. Hassabis, P. Kohli, Unveiling the predictive power of static structure in glassy systems, Nat. Phys. 16 (2020) 448–454, doi:10.1038/s41567-020-0842-8.
- [12] E.D. Cubuk, R.J.S. Ivancic, S.S. Schoenholz, D.J. Strickland, A. Basu, Z.S. Davidson, J. Fontaine, J.L. Hor, Y.-R. Huang, Y. Jiang, N.C. Keim, K.D. Koshigan, J.A. Lefever, T. Liu, X.-G. Ma, D.J. Magagnosc, E. Morrow, C.P. Ortiz, J.M. Rieser, A. Shavit, T. Still, Y. Xu, Y. Zhang, K.N. Nordstrom, P.E. Arratia, R.W. Carpick, D.J. Durian, Z. Fakhraai, D.J. Jerolmack, D. Lee, J. Li, R. Riggleman, K.T. Turner, A.G. Yodh, D.S. Gianola, A.J. Liu, Structure-property relationships from universal signatures of plasticity in disordered solids, Science 358 (2017) 1033–1037, doi:10.1126/science.aai8830.
- [13] T. Aste, M. Saadatfar, T.J. Senden, Geometrical structure of disordered sphere packings, Phys. Rev. E. 71 (2005) 061302, doi:10.1103/PhysRevE.71.061302.
- [14] A. Bunde, S. Havlin, Fractals and Disordered Systems, Springer Science & Business Media, 2012.
- [15] Q. Wang, A. Jain, A transferable machine-learning framework linking interstice distribution and plastic heterogeneity in metallic glasses, Nat Commun 10 (2019) 1–11, doi:10.1038/s41467-019-13511-9.
- [16] M.A. Klatt, J. Lovrić, D. Chen, S.C. Kapfer, F.M. Schaller, P.W.A. Schönhöfer, B.S. Gardiner, A.-S. Smith, G.E. Schröder-Turk, S. Torquato, Universal hidden order in amorphous cellular geometries, Nat. Commun. 10 (2019) 811, doi:10.1038/s41467-019-08360-5.
- [17] M. Mungan, S. Sastry, K. Dahmen, I. Regev, Networks and hierarchies: how amorphous materials learn to remember, Phys. Rev. Lett. 123 (2019) 178002, doi:10.1103/PhysRevLett.123.178002.
- [18] R.L. Jack, A.J. Dunleavy, C.P. Royall, Information-theoretic measurements of coupling between structure and dynamics in glass formers, Phys. Rev. Lett. 113 (2014) 095703, doi:10.1103/PhysRevLett.113.095703.
- [19] A. Widmer-Cooper, P. Harrowell, H. Fynewever, How reproducible are dynamic heterogeneities in a supercooled liquid? Phys. Rev. Lett. 93 (2004) 135701, doi:10.1103/PhysRevLett.93.135701.
- [20] G. Biroli, Machine learning glasses, Nat. Phys. 16 (2020) 373–374, doi:10.1038/ s41567-020-0873-1.
- [21] K.T. Butler, D.W. Davies, H. Cartwright, O. Isayev, A. Walsh, Machine learning for molecular and materials science, Nature 559 (2018) 547, doi:10.1038/s41586-018-0337-2.
- [22] E.D. Cubuk, S.S. Schoenholz, J.M. Rieser, B.D. Malone, J. Rottler, D.J. Durian, E. Kaxiras, A.J. Liu, Identifying structural flow defects in disordered solids using machine-learning methods, Phys. Rev. Lett. 114 (2015), doi:10.1103/ PhysRevLett.114.108001.
- [23] S.S. Schoenholz, E.D. Cubuk, D.M. Sussman, E. Kaxiras, A.J. Liu, A structural approach to relaxation in glassy liquids, Nat. Phys. 12 (2016) 469–471, doi:10.1038/nphys3644.
- [24] E.D. Cubuk, S.S. Schoenholz, E. Kaxiras, A.J. Liu, Structural properties of defects in glassy liquids, J. Phys. Chem. B. 120 (2016) 6139–6146, doi:10.1021/acs.jpcb. 6b02144.
- [25] D.M. Sussman, S.S. Schoenholz, E.D. Cubuk, A.J. Liu, Disconnecting structure and dynamics in glassy thin films, Proc. Natl Acad. Sci. 114 (2017) 10601– 10605, doi:10.1073/pnas.1703927114.

[26] X. Ma, Z.S. Davidson, T. Still, R.J.S. Ivancic, S.S. Schoenholz, A.J. Liu, A.G. Yodh, Heterogeneous activation, local structure, and softness in supercooled colloidal liquids, Phys. Rev. Lett. 122 (2019), doi:10.1103/PhysRevLett.122. 028001.

- [27] E. Masoero, E. Del Gado, R.J.-M. Pellenq, F.-.J. Ulm, S. Yip, Nanostructure and nanomechanics of cement: polydisperse colloidal packing, Phys. Rev. Lett. 109 (2012) 155503. doi:10.1103/PhysRevLett.109.155503.
- [28] H. Liú, S. Dong, L. Tang, N.M.A. Krishnan, G. Sant, M. Bauchy, Effects of polydispersity and disorder on the mechanical properties of hydrated silicate gels, J. Mech. Phys. Solids 122 (2019) 555–565, doi:10.1016/j.jmps.2018. 10.003.
- [29] H. Liu, L. Tang, N.M.A. Krishnan, G. Sant, M. Bauchy, Structural percolation controls the precipitation kinetics of colloidal calcium-silicate-hydrate gels, J. Phys. D: Appl. Phys. 52 (2019) 315301, doi:10.1088/1361-6463/ab217b.
- [30] E. Masoero, E.D. Gado, R.J.-M. Pellenq, S. Yip, F.-J. Ulm, Nano-scale mechanics of colloidal C-S-H gels, Soft Matter 10 (2014) 491-499, doi:10.1039/C3SM51815A.
- [31] K. Ioannidou, R.J.-M. Pellenq, E.D. Gado, Controlling local packing and growth in calcium-silicate-hydrate gels, Soft Matter 10 (2014) 1121–1133, doi:10.1039/ C3SM52232F.
- [32] S. Plimpton, Fast parallel algorithms for short-range molecular dynamics, J. Comput. Phys. 117 (1995) 1–19, doi:10.1006/jcph.1995.1039.
- [33] Y. Yu, M. Wang, D. Zhang, B. Wang, G. Sant, M. Bauchy, Stretched exponential relaxation of glasses at low temperature, Phys. Rev. Lett. 115 (2015), doi:10. 1103/PhysRevLett.115.165901.
- [34] Y. Yu, M. Wang, M.M. Smedskjaer, J.C. Mauro, G. Sant, M. Bauchy, Thermometer effect: origin of the mixed alkali effect in glass relaxation, Phys. Rev. Lett. 119 (2017) 095501, doi:10.1103/PhysRevLett.119.095501.
- [35] P. Richard, M. Nicodemi, R. Delannay, P. Ribière, D. Bideau, Slow relaxation and compaction of granular systems, Nat. Mater. 4 (2005) 121–128, doi:10.1038/ nmat1300.
- [36] D.J. Lacks, M.J. Osborne, Energy landscape picture of overaging and rejuvenation in a sheared glass, Phys. Rev. Lett. (2004) 93, doi:10.1103/PhysRevLett.93. 255501.
- [37] P. Ballesta, G. Petekidis, Creep and aging of hard-sphere glasses under constant stress, Phys. Rev. E. 93 (2016) 042613, doi:10.1103/PhysRevE.93.042613.
- [38] T. Gibaud, N. Dagès, P. Lidon, G. Jung, L.C. Ahouré, M. Sztucki, A. Poulesquen, N. Hengl, F. Pignon, S. Manneville, Rheoacoustic gels: tuning mechanical and flow properties of colloidal gels with ultrasonic vibrations, Phys. Rev. X. 10 (2020) 011028, doi:10.1103/PhysRevX.10.011028.
- [39] V. Grenard, T. Divoux, N. Taberlet, S. Manneville, Timescales in creep and yielding of attractive gels, Soft Matter 10 (2014) 1555, doi:10.1039/ c3sm52548a.
- [40] C. Liu, K. Martens, J.-L. Barrat, Mean-field scenario for the athermal creep dynamics of yield-stress fluids, Phys. Rev. Lett. 120 (2018) 028004, doi:10.1103/PhysRevLett.120.028004.
- [41] M.L. Falk, J.S. Langer, Dynamics of viscoplastic deformation in amorphous solids, Phys. Rev. E 57 (1998) 7192–7205, doi:10.1103/PhysRevE.57.7192.
- [42] A. Stukowski, Visualization and analysis of atomistic simulation data with OVITO-the open visualization tool, Model. Simul. Mater. Sci. Eng. 18 (2010) 015012, doi:10.1088/0965-0393/18/1/015012.
- [43] N. Mousseau, L.K. Béland, P. Brommer, J.-.F. Joly, F. El-Mellouhi, E. Machado-Charry, M.-.C. Marinica, P. Pochet, The activation-relaxation technique: ART Nouveau and Kinetic ART, J. Atom., Mol. Optic. Phys. 2012 (2012) 1–14, doi:10. 1155/2012/925278.
- [44] L. Tang, G. Ma, H. Liu, W. Zhou, M. Bauchy, Bulk metallic glasses' response to oscillatory stress is governed by the topography of the energy landscape, J. Phys. Chem. B. (2020) acs.jpcb.0c08794, doi:10.1021/acs.jpcb.0c08794.
- [45] L. Tang, H. Liu, G. Ma, T. Du, N. Mousseau, W. Zhou, M. Bauchy, The energy landscape governs ductility in disordered materials, Mater. Horiz. (2021), doi:10.1039/D0MH00980F.
- [46] C.E. Maloney, A. Lemaître, Amorphous systems in athermal, quasistatic shear, Phys. Rev. E 74 (2006), doi:10.1103/PhysRevE.74.016118.
- [47] C.E. Maloney, D.J. Lacks, Energy barrier scalings in driven systems, Phys. Rev. E. 73 (2006) 061106, doi:10.1103/PhysRevE.73.061106.
- [48] C.M. Bishop, Pattern Recognition and Machine Learning, Springer, New York, 2006.
- [49] A. Nicolas, E.E. Ferrero, K. Martens, J.-.L. Barrat, Deformation and flow of amorphous solids: insights from elastoplastic models, Rev. Mod. Phys. 90 (2018) 045006, doi:10.1103/RevModPhys.90.045006.
- [50] J.C. Maxwell, L. On the calculation of the equilibrium and stiffness of frames, London, Edinburgh, Dublin Philos. Mag. J. Sci. 27 (1864) 294–299, doi:10.1080/14786446408643668.
- [51] C.F. Moukarzel, Isostatic phase transition and instability in stiff granular materials, Phys. Rev. Lett. 81 (1998) 1634–1637, doi:10.1103/PhysRevLett. 81.1634.
- [52] B. Keshavarz, T. Divoux, S. Manneville, G.H. McKinley, Nonlinear viscoelasticity and generalized failure criterion for polymer gels, ACS Macro Lett. 6 (2017) 663–667, doi:10.1021/acsmacrolett.7b00213.